10

Internal Waves in Laboratory Experiments

Bruce Sutherland[1], Thierry Dauxois[2], and Thomas Peacock[3]

10.1. INTRODUCTION

Since the realization by physical oceanographers that transport and mixing by internal waves are an important component of the thermohaline circulation, there has been a resurgence in interest in their dynamics [*Polzin et al.*, 1997; *Munk and Wunsch*, 1998; *Ledwell et al.*, 2000]. Consequent studies have been designed to examine mechanisms for wave generation and interaction with topography. Theoretical studies have examined the means by which energy from the moon forcing the barotropic tide might be converted into internal wave energy as a consequence of oscillatory stratified flow over topography. This began with the pioneering studies of *Zeilon* [1912] and *Baines* [1974, 1982] and have since been extended, though still in the realm of linear theory, to examine the influence of more complex topography and stratification [*Balmforth et al.*, 2002; *Llewellyn-Smith and Young*, 2002; *Bühler and Muller*, 2007]. Related to these is the examination of scattering of internal waves by topography in which incident low-mode internal waves generate an oscillatory flow over topography that launches higher-mode internal waves [*Larsen*, 1969; *Robinson*, 1969; *Sandstrom*, 1969].

Just as an oscillatory flow over a rigid body generates internal waves, so does an oscillating body generate internal waves in otherwise stationary fluid. The particular circumstance of internal waves generated by oscillating cylinders and spheres has garnered much attention [*Görtler*, 1943; *Mowbray and Rarity*, 1967; *Thomas and Stevenson*, 1972; *Voisin*, 1991, 1994; *Hurley*, 1997; *Hurley and Keady*, 1997]. Even with such simple geometries and despite neglecting Coriolis effects, this work has revealed the importance of including viscosity to resolve singularities that occur along tangents to the oscillating body in the along-beam direction.

More recently, in the study of tidally generated internal waves, attention has turned to faster time-scale processes in which large-amplitude internal wave packets are generated during one cycle of the tide. This work extends earlier studies of steady uniformly stratified flow over topography (e.g., see *Baines* [1995]) to include consideration of nonuniform stratification and large-amplitude topography. Oceanographers have focused primarily upon the generation, propagation, and dissipation of internal solitary waves at the thermocline [*Pinkel*, 2000; *Klymak and Gregg*, 2004; *Klymak et al.*, 2006; *Li and Farmer*, 2011; *Alford et al.*, 2011].

By exploring large-amplitude and viscous effects, the results of laboratory experiments have often challenged existing theory. For example, they have revealed the importance of nonlinear processes in the scattering of internal waves from large-amplitude topography [*Peacock et al.*, 2009], they have demonstrated the importance of the viscous boundary layer in the generation of internal waves from oscillating bodies [*Sutherland and Linden*, 2002; *Flynn et al.*, 2003], and they have shown that boundary layer separation in stratified flow over steep topography reduces the effective topographic height while generating turbulence and internal waves in the lee of localized topography [*Baines and Hoinka*, 1985; *Sutherland*, 2002; *Aguilar and Sutherland*, 2006].

Laboratory experiments have entered a renaissance due to digitization technology, advancement in lasers and computer-controlled equipment, and increases in computational memory and speed, which have created valuable new analysis tools such as particle image velocimetry (PIV) and laser-induced fluorescence (LIF). As a result,

[1]*Departments of Physics and of Earth & Atmospheric Sciences, University of Alberta, Edmonton, Alberta, Canada.*

[2]*Laboratoire de Physique, École Normale Supérieure, Lyon, France.*

[3]*Department of Mechanical Engineering, Massachusetts Institute of Technology, Cambridge, Massachusetts, United States of America.*

Modeling Atmospheric and Oceanic Flows: Insights from Laboratory Experiments and Numerical Simulations,
First Edition. Edited by Thomas von Larcher and Paul D. Williams.

it is now possible to make nonintrusive measurements of velocity and concentration in two and even three dimensions. These tools have provided new insights into problems involving turbulence and mixing that remain a challenge in computational fluid dynamics.

However, the study of stratified fluids remains an experimental challenge because light typically refracts differently through fluids of varying density. This can distort and smear the apparent positions of particles used in PIV and so lead to spurious predictions of flow speeds. On the other hand, the very fact that density and refractive index are related has provided other means to examine nonintrusively the structure of stratified fluid flow.

One visualization tool used in laboratory experiments of salt-stratified fluids is the shadowgraph. In this, a light source placed far behind the test section shines through the stratified fluid landing upon a translucent surface such as Mylar. At interfaces where the density rapidly changes, the light focuses and defocuses as it bends relatively more or less while passing through fluid of varying salinity and, hence, varying refractive index. If density variations due to internal waves are gradual, focusing may not be evident. The shadowgraph proves particularly useful in the examination of approximately two-layer fluids, in which case light focusing at the interface can be used to track the motion of interfacial waves. For internal waves in uniformly stratified fluid, the shadowgraph is particularly effective in the examination of waves that are close to breaking, as shown in Figure 10.1. In this experiment [*Koop and McGee*, 1986], sinusoidal topography is towed leftward beneath a shear flow whose speed increases leftward with height. At middepth in the experiments the waves encounter a critical level, where the background flow speed is close to the towing speed of the hills.

Another method taking advantage of the relationship between refractive index and density is called "schlieren" [*Schardin*, 1942; *Settles*, 2001]. In the traditional approach, light reflected from a parabolic mirror passes through a test section before striking a second parabolic mirror that refocuses the light. A knife edge at the focus acts as a filter on spurious signals, thus revealing index-of-refraction-dependent structures within the test section.

Mowbray and Rarity [1967] were the first to use traditional schlieren methods to visualize internal waves generated by a cylinder oscillating at a fixed frequency, ω. Provided ω was sufficiently small, they observed that the waves emanated vertically and horizontally from the cylinder in a cross pattern, as shown in Figure 10.2.

In this experiment, the fluid was a uniformly stratified salt solution whose density decreased linearly with height. The stratification can be represented by the buoyancy frequency N, defined in the Boussinesq approximation by

$$N^2 = -\frac{g}{\rho_0}\frac{d\bar{\rho}}{dz}. \tag{10.1}$$

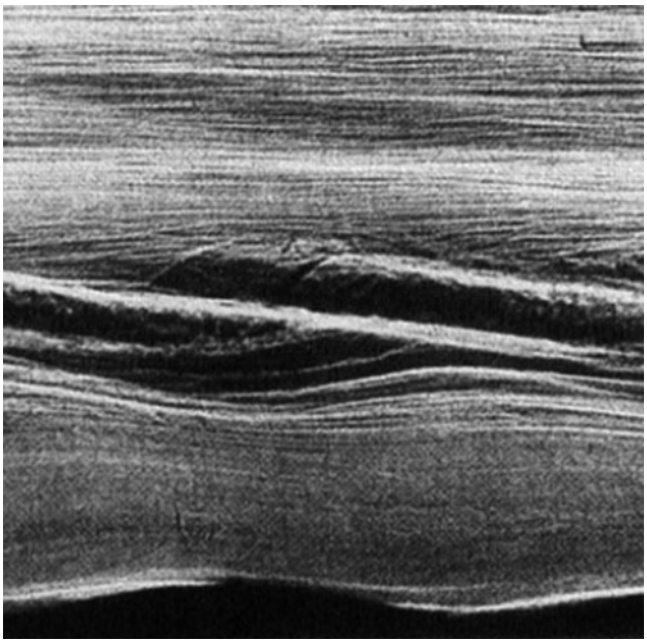

Figure 10.1. Internal wave breaking near a critical layer as visualized by shadowgraph. Reprinted from Figure 7 of *Koop and McGee* [1986].

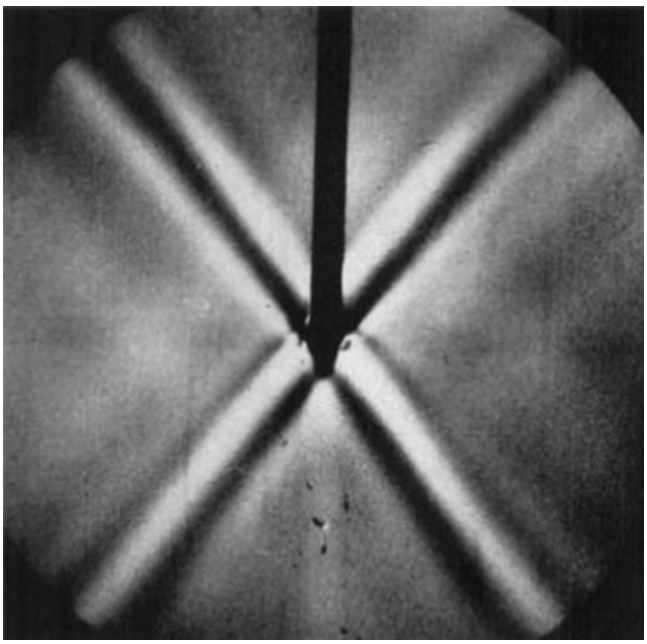

Figure 10.2. Pattern of internal waves generated by an oscillating cylinder as visualized by conventional schlieren methods. Reproduced from Plate 1(6) of *Mowbray and Rarity* [1967].

Here $\bar{\rho}(z)$ is the ambient density, ρ_0 is the characteristic density (e.g., that for fresh water at room temperature), and g is the acceleration of gravity. In agreement with the predicted dispersion relation of internal waves, *Mowbray*

and Rarity [1967] found that the arms of the cross-pattern of waves formed a fixed angle Θ from the vertical that was related to the ratio of ω to N by $|\Theta| = \cos^{-1}(\omega/N)$.

Color filters have allowed schlieren to be more quantitative [*Howes*, 1984; *Teoh et al.*, 1997; *Chashechkin*, 1999]. But the expense and physical constraints imposed by the need for well-aligned pairs of parabolic mirrors has limited the use of schlieren until recently.

Schlieren technology has advanced enormously since the mid-1990s. As a result of digitization technology and computers, "synthetic schlieren" was developed as an inexpensive, versatile and, most importantly, quantitative tool for sensitively measuring density perturbations in stratified fluids.

In what follows we examine how synthetic schlieren has been used to test theory and to develop new insights into the dynamics of internal waves. In the process we review an analysis method for separating out waves propagating in different directions and we describe a recently developed mechanism for generating waves that does not suffer some of the drawbacks of oscillating or towed rigid objects.

Section 10.2 briefly discusses how synthetic schlieren visualizes disturbances in a fluid through contrasting snapshots taken by a digital camera looking through the fluid at a black-and-white image of lines or dots. If the disturbances are small, the displacements of objects in the image can be computed and, from these, the magnitude of the disturbance calculated. This is described in Section 10.3 with the assumption that the disturbance in the tank is uniform across the line of sight. The treatment of axisymmetric and fully three-dimensional disturbances is described in Section 10.4. Other advances in generating internal waves and analyzing them using PIV are described in Section 10.5. Future directions are described in Section 10.6.

10.2. QUALITATIVE USE OF SYNTHETIC SCHLIEREN

Synthetic schlieren [*Dalziel et al.*, 2000] makes away with the need for parabolic mirrors to straighten and refocus a localized light source. Instead, a camera is focused upon an image behind a tank filled with salt-stratified fluid.[1] Disturbances in the fluid displace isopycnal surfaces and so locally change the refractive index of the salt water through which light passes from a point on the image through the tank to the camera. The image apparently distorts as a result.

For example, Figure 10.3 shows how qualitative synthetic schlieren observes distortions of an image of horizontal black-and-white lines resulting when a set of model sinusoidal "hills" are towed from left to right over the surface of a tank filled with uniformly stratified fluid.

In the initial image, shown in Figure 10.3a, the hills immersed in the ambient are apparent near the top of the frame. The black-and-white lines are not in the tank, however. The image is situated approximately 10 cm behind the tank. After the hills are set in motion, various disturbances in the ambient can be seen as a result of the distortion of the image (Figure 10.3b). In the lee of each hill, boundary layer separation results in large perturbations that warp and blur the lines. Furthermore, below the hills the eye can barely make out smaller undulations of lines in the image.

These alterations can be enhanced through digital image processing. Each snapshot can be represented as an array of pixels with each pixel given a number corresponding to its intensity (e.g., 0 for black, 1 for white, and in between for gray). The image in Figure 10.3c is produced by taking the difference of the digitized snapshot in (b) from that in (a), then taking the absolute value and multiplying the result by an enhancement factor, typically 10. Thus even small changes to the image become obvious.

One advantage of synthetic schlieren is that its sensitivity can be increased by widening the distance between the test section and the image behind it. For example, it is easy to observe heat rising off one's hand if the image is several meters away.

10.3. SPANWISE-UNIFORM DISTURBANCES

10.3.1. Quantitative Synthetic Schlieren

When light passes through a medium whose refractive index changes in space, it is deflected in a manner well predicted by Snell's law. In the particular case of stably stratified fluid, the density ρ and hence refractive index n change with height z. The path of light passing in the y direction through the fluid at a small angle to the vertical from the y axis is given by [*Sutherland et al.*, 1999]

$$\frac{d^2z}{dy^2} \simeq \frac{1}{n_0}\frac{\partial n}{\partial z}. \tag{10.2}$$

Here n_0 is the characteristic refractive index of the fluid (e.g., $n_0 = 1.3330$ for pure water).

In uniformly stratified fluid, the vertical gradient of the refractive index can be related to the vertical density gradient:

$$\frac{\partial n}{\partial z} = \frac{dn}{d\rho}\frac{\partial \rho_T}{\partial z}. \tag{10.3}$$

Here ρ_T denotes the sum of the ambient density $\bar{\rho}(z)$ and the perturbation density $\rho(\vec{x}, t)$.

[1] Synthetic schlieren has also been called "background oriented schlieren" by *Meier* [2002], who used it to visualize and measure shock waves in air.

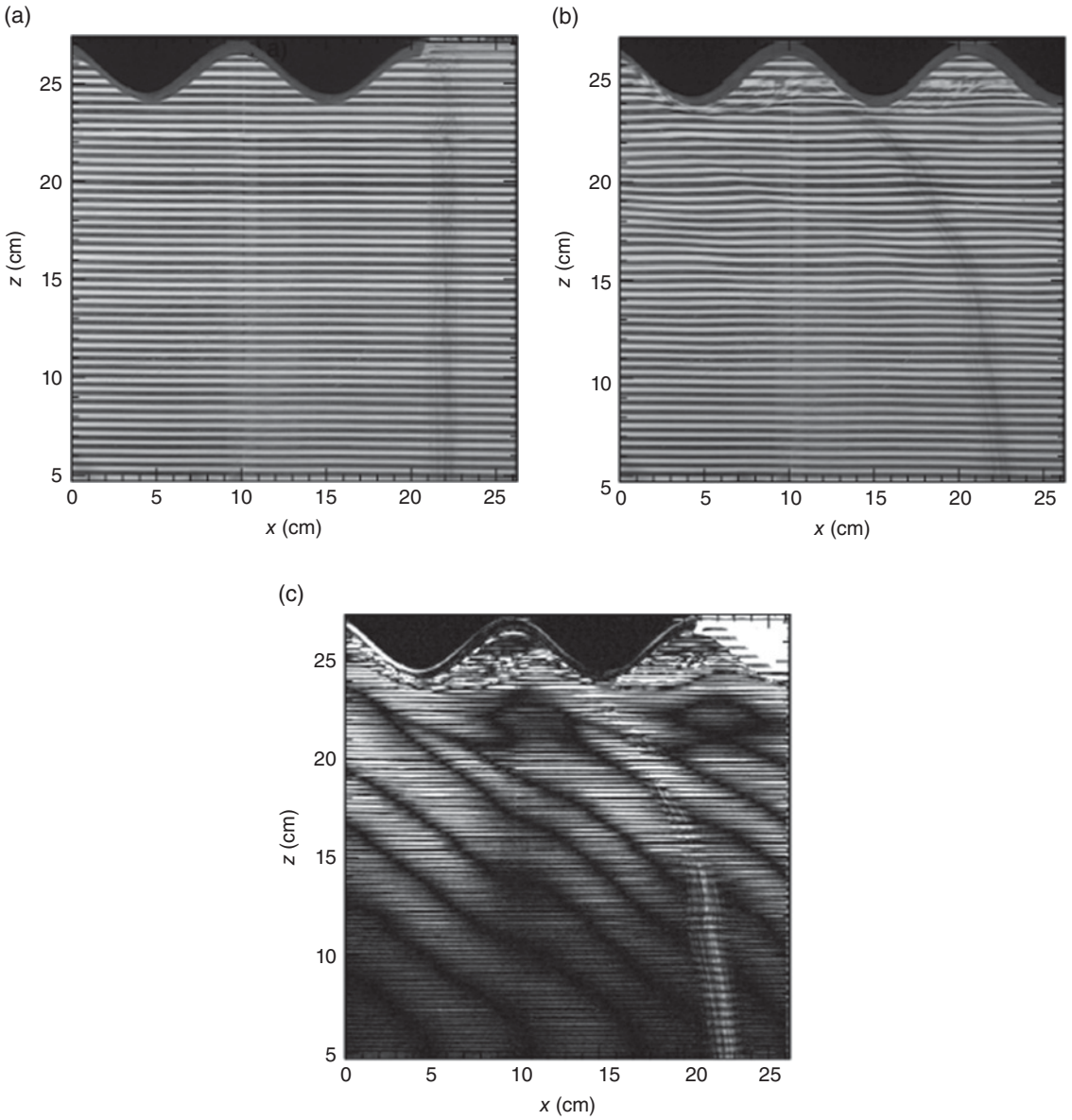

Figure 10.3. (a) Side view looking through tank filled with salt-stratified fluid with model inverted sinusoidal hills at the surface and an image of horizontal black-and-white lines placed behind the tank. (b) Side view after hills have been towed slowly a distance of one hill width. (c) Qualitative synthetic schlieren image produced by taking the absolute value of the difference of the digitized images shown in (a) and (b). Also evident in (a) and (b) is a dark vertical streak above $x \simeq 20\,\text{cm}$. This is a vertical dye line suspended in the fluid itself. Its displacement can be used to determine mean horizontal flow, which is retrograde to the towing direction of the hill.

In computing image displacements, it is sometimes more intuitive to compute them in terms of the squared buoyancy frequency rather than density gradients. The local stratification resulting from both the background and perturbation density is expressed by the total squared buoyancy frequency:

$$N_T{}^2 = -\frac{g}{\rho_0}\frac{\partial \rho_T}{\partial z}. \tag{10.4}$$

Thus vertical variations of the refractive index can be written in terms of N_T by

$$\frac{\partial n}{\partial z} = -n_0 \gamma N_T{}^2, \tag{10.5}$$

in which the coefficient γ is defined so that

$$\gamma \equiv \frac{1}{g}\frac{\rho_0}{n_0}\frac{dn}{d\rho} \simeq 1.878 \times 10^{-4}\ \text{s}^2/\text{cm}. \tag{10.6}$$

The rightmost empirical approximation assumes relatively weak concentrations of sodium chloride solutions [*Weast*, 1981].

Combining equations (10.2) and (10.5), we find that light follows a parabolic path when passing through a uniform stratification at a scant angle from the horizontal such that

$$z(y) = z_i + y \tan \phi_i - \frac{1}{2}\gamma N_T{}^2 y^2, \qquad (10.7)$$

in which z_i is the height and ϕ_i is the angle at which the light ray enters the tank, In deriving (10.7), we have assumed that N_T is independent of y, which is the case for spanwise uniform disturbances in a tank. This assumption will be relaxed below in the consideration of axisymmetric and fully three-dimensional disturbances.

Synthetic schlieren is usually employed to measure perturbations to the ambient. Directly, it measures how the squared buoyancy frequency changes as a result of the compression and stretching of isopycnal surfaces. Over a distance $y = L_T$, light is deflected vertically by

$$\Delta z = -\frac{1}{2}\gamma \, \Delta N^2 \, L_T{}^2, \qquad (10.8)$$

in which

$$\Delta N^2 \equiv N_T{}^2 - N^2 = -\frac{g}{\rho_0}\frac{\partial \rho}{\partial z} \qquad (10.9)$$

is the change in the squared buoyancy due to the density perturbation ρ.

For example, if internal waves compress isopycnals so that the ambient N^2 locally increases by 10% from 1.0 to 1.1 s^{-2}, then the light deflects by 0.04 mm crossing a 20 cm wide tank. This is a small but discernible displacement that can be captured by a digital camera with sufficiently high resolution.

The apparent deflection is larger if the image is placed some distance behind the tank. Not only is the light deflected downward if the stratification increases, but also the angle of the light ray at the tank wall changes. So the apparent image displacement magnifies linearly as the image is moved further away.

Assuming the tank walls are negligibly thin, one can predict the total displacement of light from an object a distance L_o from one side of the tank to a camera on the other side of the tank to be

$$\Delta z(\Delta N^2) \simeq -\frac{1}{2}\gamma \, \Delta N^2 \, L_T{}^2 - \frac{n_0}{n_a}\gamma \, \Delta N^2 \, L_o L_T, \quad (10.10)$$

in which n_a is the refractive index of air and ϕ_0 is the angle from the horizontal at which light enters the camera from the object.

In the example above, if we now suppose the image is 20 cm behind the tank, then the displacement of the light path is 0.14 mm, which is much more easily discernible. If one pixel of the camera has a vertical resolution of 0.5 mm, then the disturbance in the tank will shift the image by about a third of a pixel, which can easily be observed by the change of intensity of light emanating from the edge of a line.

Through (10.10), we have found the forward equation in which known changes to the stratification enables us to predict the vertical displacement of a point in an object as seen by a camera looking through the stratified fluid. In the derivation of (10.7), because we have assumed the disturbance is spanwise uniform, it is a trivial matter to invert (10.10) so that an observed vertical displacement in an image can predict the change in the stratification:

$$\Delta N^2 \simeq -\Delta z \, \frac{1}{\gamma}\left[\frac{1}{2}L_T{}^2 + L_o L_T \frac{n_0}{n_a}\right]^{-1}. \qquad (10.11)$$

If part of an image appears to deflect downward, it means that the stratification between it and the camera has locally become stronger.

This result is straightforwardly applied to the circumstance in which a camera looks through a tank at an image of horizontal black-and-white lines, as is the case in Figure 10.3. Even if density perturbations result in image distortions that shift the lines by a fraction of their width (which, in fact, is ideal if you wish easily to compute the line displacement), then (10.11) immediately predicts the change to the squared buoyancy frequency.

More processing is required if the line is displaced significantly. The calculation of displacements is even more difficult if the lines become magnified or contracted because second derivatives of the refractive index become significant (in which case a shadowgraph becomes the more useful, if qualitative, tool). The method breaks down entirely, as within the valleys of the model hills in Figure 10.3b, when the lines blur due to three-dimensional mixing.

The examination of an image of lines provides a relatively easy method to calculate small vertical displacements in an image and hence ΔN^2. But a far more informative, though computationally more intensive, application uses an image of dots [*Dalziel et al.*, 2000]. For example, Figure 10.4 shows a qualitative synthetic schlieren image produced with a beam of internal waves from an oscillating cylinder that passes in front of an image of regularly spaced black circles on a white background. The difference image is shown, analogous to that in Figure 10.3.

The cat-eye-like patterns have a black portion near the center of the dot surrounded on two sides by white, indicating how the dot shifted both horizontally and vertically as a result of internal waves passing between the camera and image. The angle and eccentricity of the

Figure 10.4. Pattern of internal waves generated by an oscillating cylinder in the upper left-hand corner as visualized by qualitative synthetic schlieren applied to a pattern of equally spaced dots behind the tank. Adapted from Figure 7c of *Dalziel et al.* [2000].

resulting elliptical disturbance give both components of the perturbation density gradient. Multiplying by $-g/\rho_0$, as in equation (10.9), the perturbation density gradient may be recast in terms of the perturbation squared buoyancy frequency: $(\Delta N^2{}_x, \Delta N^2{}_z) \equiv -(g/\rho_0)\,\nabla\rho$.

Alternately, if the image of dots is randomly distributed, then particle image velocimetry techniques can be used to measure horizontal and vertical displacements of portions of the image [*Dalziel et al.*, 2000]. Assuming the disturbance in the ambient is uniform along the line of sight, each displacement field can be used to find the perturbation density gradient. This can be integrated to compute the perturbation density field, as shown in Figure 10.5.

10.3.2. Separating Up from Down and Left from Right

A powerful analysis tool related to Hilbert transforms can be used to distinguish upward from downward propagating internal waves and simultaneously distinguish leftward from rightward propagating waves [*Mercier et al.*, 2008]. This can be applied to vertical or horizontal time series constructed from simulations, in situ observations, and laboratory experiments. Whether spanwise uniform, axisymmetric, or fully three dimensional, the method can distinguish propagation direction in the spatial component of the time series. Its application will be discussed here in the context of internal waves generated by an oscillating cylinder.

Consider Figure 10.6, which shows the ΔN^2 field computed using synthetic schlieren for an oscillating cylinder experiment. Imagining a Cartesian grid superimposed on the wave field with the origin at the center of the disturbance, the four arms of the cross consist of upward propagating waves emanating rightward and leftward in the first and second quadrants, respectively, and of downward propagating waves emanating leftward and rightward in the third and fourth quadrants, respectively. Hilbert transforms can extract each arm of the cross, as shown in Figure 10.7.

In application, the method does not formally compute the Cauchy principle value integral associated with a Hilbert transform. Instead, it employs filtering of Fourier transform images, specifically those of time series of the disturbances. For example, consider a synthetic schlieren employing an image of horizontal black-and-white lines behind a tank. During the evolution of a spanwise-uniform disturbance, one can compute $\Delta N^2(x, z, t)$, in which z is vertical, x is the along-tank coordinate, and t is time. Fixing an arbitrary horizontal location X, one can construct the vertical time series $\Delta N^2(z, t; x = X)$. Taking the double fast Fourier transform first in t and then in z gives the complex series coefficients $\widehat{\Delta N^2}(k_z, \omega)$, in which k_z is the vertical wave number and ω is the frequency.

To extract upward propagating disturbances, we use the fact that the group velocity of internal waves is positive if the vertical wave number is negative. So we set $\widehat{\Delta N^2}$ to zero if k_z is positive and leave the field untouched otherwise. An inverse Fourier transform then produces a filtered field $\Delta N^2{}_{\uparrow}(z, t; x = X)$ with only upward propagating disturbances. This process can be repeated at different horizontal locations until the entire evolution field of upward propagating disturbances is reproduced: $\Delta N^2{}_{\uparrow}(x, z, t)$.

We can similarly extract rightward propagating waves by Fourier transforming horizontal time series at successive $z = Z$, setting the coefficients of negative horizontal wave numbers to zero and then inverse transforming. The result of applying this to $\Delta N^2{}_{\uparrow}$, for example, gives the up and rightward wave beam shown in the top-left panel of Figure 10.7.

10.3.3. Partial Transmission and Reflection

The use of the Hilbert transform method described above has proven to be particularly useful in the study of internal wave propagation in nonuniformly stratified fluid. The intuitive understanding of their propagation is based upon ray theory, which assumes the small-amplitude wavepackets are quasi-monochromatic and that the background varies slowly compared to the wavelength [e.g., see *Lighthill*, 1978; *Sutherland*, 2010]. In particular, in a stationary fluid this predicts that waves reflect from a level

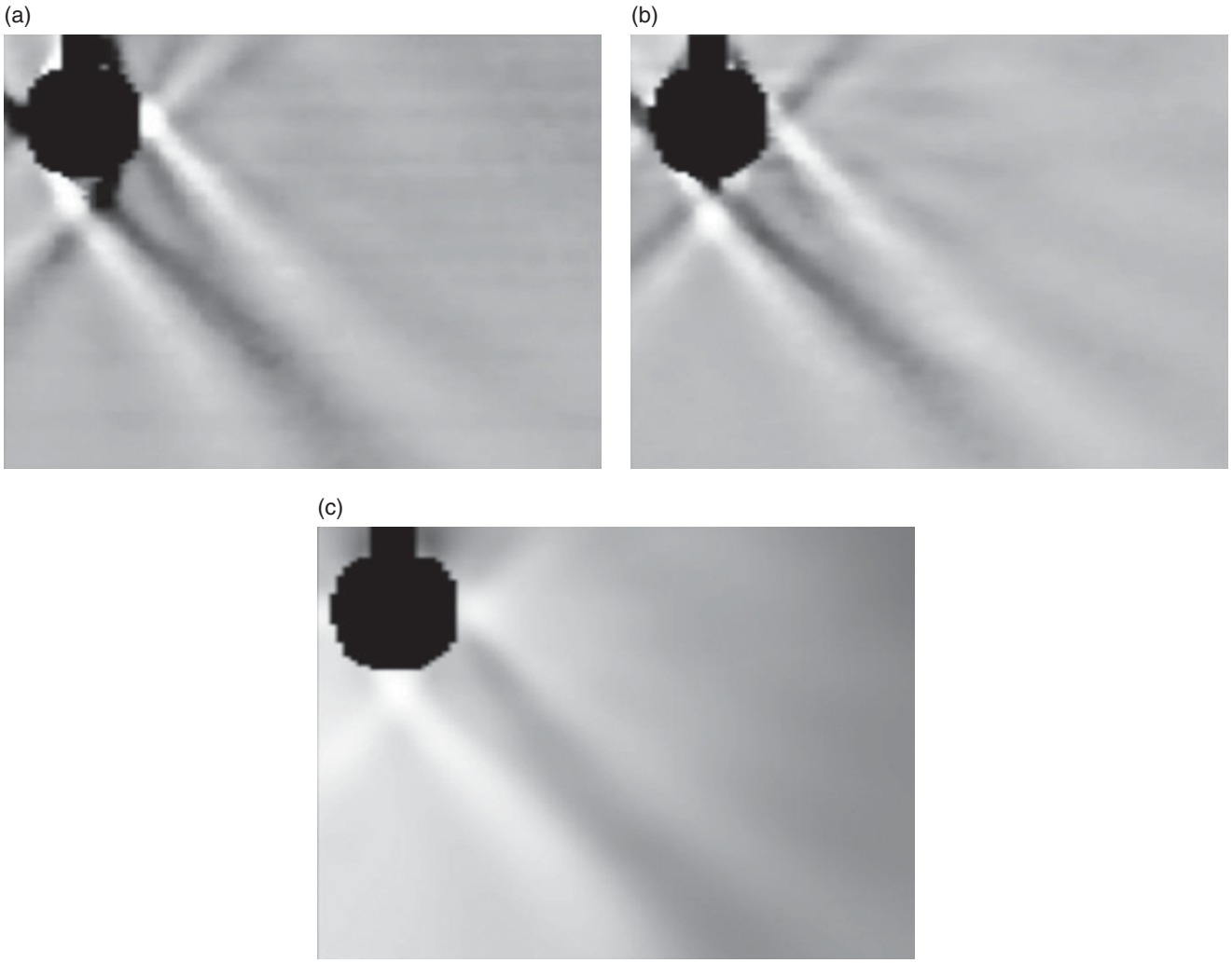

Figure 10.5. Quantitative synthetic schlieren applied to the circumstance shown in Figure 10.4, in which (a) the horizontal displacement of dots behind the tank is used to compute the (assumed spanwise-uniform) horizontal perturbation density gradient of fluid in the tank, as indicated by intensity of the gray scale. (b) Vertical dot displacements are used to compute the vertical density gradient. (c) The two components of the density gradient are integrated to find the perturbation density field. Reproduced from Figure 13 of *Dalziel et al*. [2000].

where the background buoyancy frequency is less than the wave frequency.

Following a theoretical approach analogous to that used in thin-film optics for light or in quantum mechanics for electrons, *Sutherland and Yewchuk* [2004] showed that internal waves can partially transmit (i.e., "tunnel") through a weakly stratified layer provided it is thin compared to the horizontal wavelength of the incident waves. For piecewise constant profiles of the background buoyancy frequency, they predicted the transmission coefficient T as a function of the relative frequency of the waves, ω/N_0, and their relative horizontal wave number $k_x L$ in which N_0 is the far-field buoyancy frequency and L is the depth of the thin stratified layer with buoyancy frequency N_1. The predictions are shown in Figure 10.8 for the cases of an unstratified layer, a weakly stratified layer, and a strongly stratified layer.

Counter to intuition based upon ray theory, one sees in particular that waves can partially reflect from a strongly stratified layer even though their frequency is always smaller than the background buoyancy frequency.

Of course, the phenomenon is well known in optics. Indeed, *Mathur and Peacock* [2010] made the analogy between internal waves and light showing that they behave like a Fabry-Perot multiple-beam interferometer. The resulting resonance of internal waves in a localized region of enhanced stratification was demonstrated in laboratory experiments, shown in Figure 10.9.

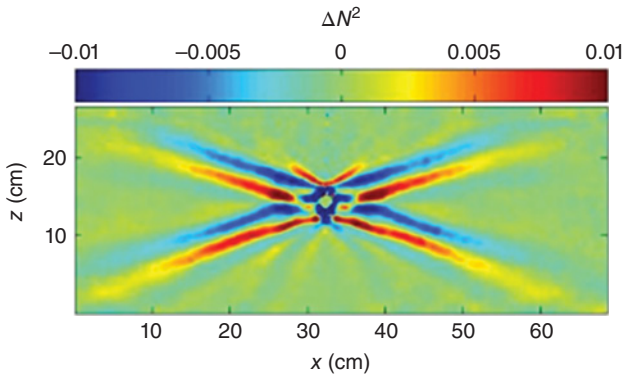

Figure 10.6. Change in the background squared buoyancy frequency (ΔN^2) due to internal waves generated by an oscillating cylinder, as measured by quantitative synthetic schlieren. The left image shows a snapshot of the ΔN^2 field; the right image shows the amplitude envelope of the wave beams. Reproduced from Figure 2 of *Mercier et al.* [2008].

The transmission of a small-amplitude wavepacket through arbitrary stratification and background flow can be computed through the solution of the Taylor-Goldstein equation [*Nault and Sutherland*, 2007, 2008]. These results were compared with laboratory experiments of internal waves incident upon a pycnocline [*Mathur and Peacock*, 2009] and of internal wave beams incident upon a weakly stratified layer [*Gregory and Sutherland*, 2010]. Using the Hilbert transform method, the incident, reflected, and transmitted waves could be distinguished and so transmission and reflection coefficients could be computed. Theory was found to be consistent with the experiments, but there was great sensitivity of the predicted transmission coefficient to the details of the stratification. For example, referring to Figure 10.8b with $\omega \simeq 0.8N$, one sees that the transmission coefficient increases rapidly from 0.4 to 1 as $k_x L$ increases from 0.7 to 1. And so, uncertainty in the measurement of k_x greatly increases the uncertainty in the predicted transmission. Likewise, with smooth N^2 profiles, the predicted transmission coefficient sensitively depends upon the smoothness of N, particularly if the incident wave frequency is close to the minimum value of N [*Gregory and Sutherland*, 2010]. For those intending to use theory to predict internal wave transmission, these experiments emphasize the importance of performing an error analysis for both incident internal wave properties and the structure of the ambient.

10.4. NON-SPANWISE-UNIFORM DISTURBANCES

The quantitative uses of synthetic schlieren described above assumed that any disturbances in the stratified fluid were uniform across the width of the tank. With this assumption, it was straightforward to relate displacements of images to changes in stratification through equation (10.10). It was likewise trivial to invert this equation and so infer changes in the stratification knowing the measured displacements, as in equation (10.11).

If disturbances are not spanwise uniform, one can still use Snell's law to write down expressions for the apparent displacement of an image due to light passing

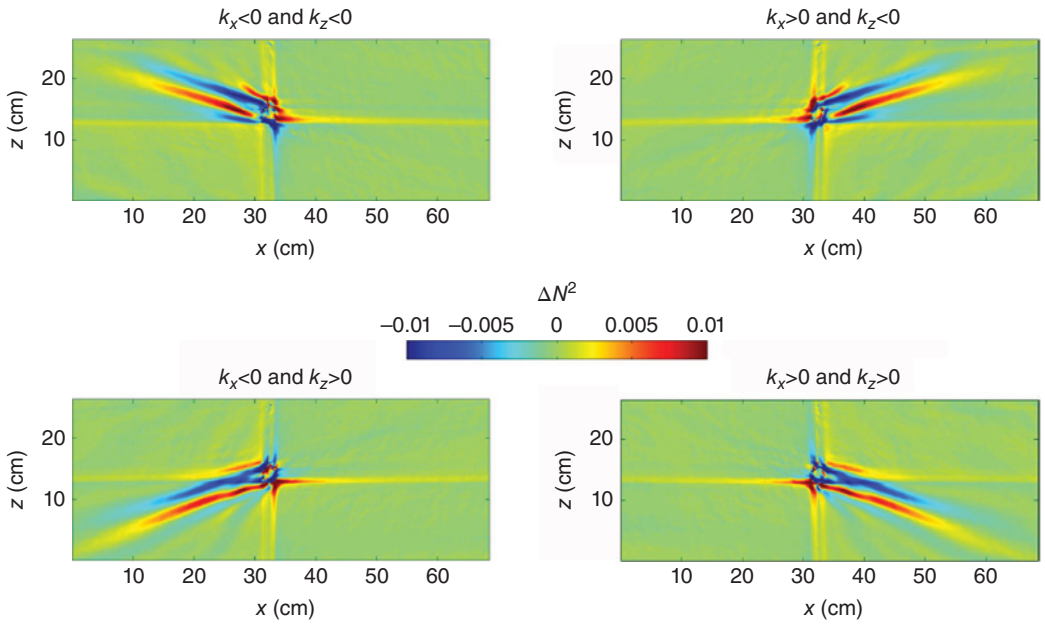

Figure 10.7. The four arms of the cross shown in Figure 10.6 determined by Fourier implementation of the Hilbert transform. Reproduced from Figure 3 of *Mercier et al.* [2008].

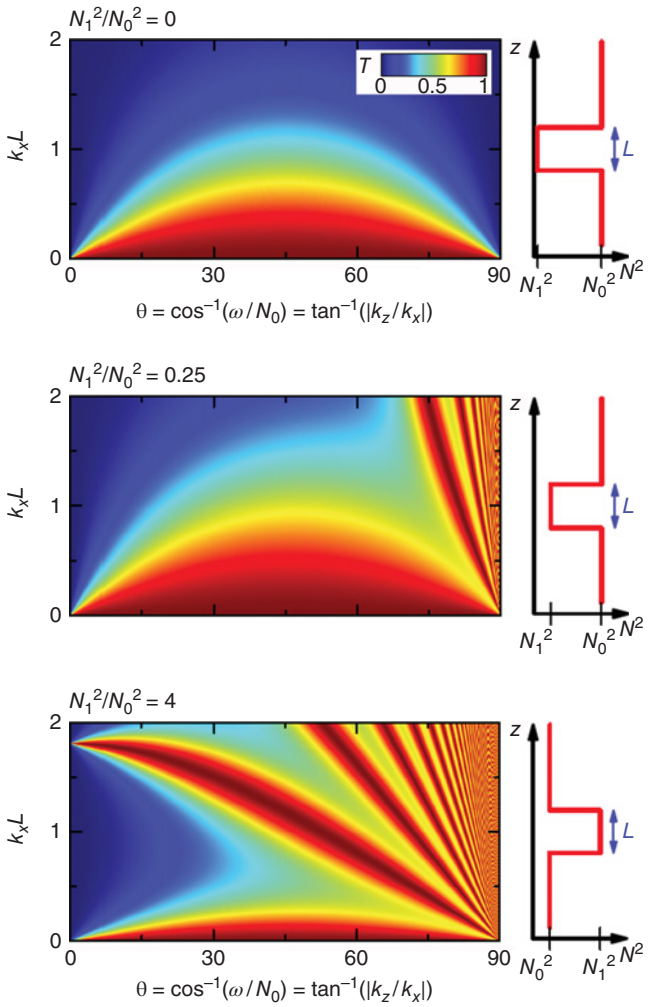

Figure 10.8. Predicted transmission coefficient for monochromatic internal waves of frequency ω and horizontal wave number k_x incident upon a region of depth L where the ambient buoyancy frequency is N_1 instead of N_0. Adapted from Figure 1 of *Sutherland and Yewchuk* [2004].

through fluid with known varying density (hence with known varying refractive index). The challenge is to invert this formula to find the change in stratification for given observed displacements.

For axisymmetric disturbances about a vertical axis, the procedure amounts to inverting a square matrix to determine $\nabla\rho$ from observed displacements of an image. For fully three-dimensional disturbances, tomographic inversion techniques are needed to reconstruct $\nabla\rho$ from displacements observed from multiple perspectives.

10.4.1. Axisymmetric Synthetic Schlieren

We consider the simplest case of reconstructing ΔN^2 from observed vertical displacements of an image, Δz [*Onu et al.*, 2003]. First we consider the vertical displacements at a fixed time and at a fixed height, so that $\Delta z(x)$ is taken to be a function only of the along-tank distance x. We seek the corresponding value of $\Delta N^2(r)$, which is assumed to be axisymmetric, varying with radius r.

The inversion problem begins with representing the along-tank direction by $n + 1$ discrete points $x_i = i\,dx$ for $i = 0, \ldots, n$ and by discretizing the radial disturbances by concentric rings of outer radius $r_j = (j + 1/2)\,dr$. So that the inversion problem is well posed, we take $dr \equiv dx$ and we set $j = 0, \ldots, n$, in which $j = 0$ signifies the innermost circle. The correspondence of the x and r coordinate systems is shown in Figure 10.10.

We assume that ΔN^2 is constant within each annulus in the central circle. And so we denote $(\Delta N^2)_0 = \Delta N^2$ for $0 \le r < dr/2$, $(\Delta N^2)_1 = \Delta N^2$ for $dr/2 \le r < 3\,dr/2$, $(\Delta N^2)_2 = \Delta N^2$ for $3\,dr/2 \le r < 5\,dr/2$, etc. Outside the outermost ring we assume the ambient is undisturbed so that $\Delta N^2 = 0$.

We now consider the path of light passing in the y direction from the far side of the tank through the disturbance field to the side of the tank nearest the camera (i.e., from top to bottom of the schematic in Figure 10.10).

Given values of ΔN^2 in each ring, we integrate equations (10.2) and (10.5), summing the discretized equations to determine the vertical position of light, $z(y)$, as it crosses each annulus. Doing so requires computing in advance the distance dy_{ij} that light from location x_i crosses the jth annulus (with the zeroth "annulus" being the central circle). Although they could be computed analytically, these geometric distances are straightforwardly determined by a numerical algorithm.

The result of the forward problem is a matrix set of equations,

$$\overrightarrow{\Delta z} = \mathbf{G}\,\overrightarrow{\Delta N^2}, \tag{10.12}$$

in which $\overrightarrow{\Delta z}$ is the transpose of $(\Delta z(0), \Delta z(x_1), \ldots, \Delta z(x_n))$, $\overrightarrow{\Delta N^2}$ is the transpose of $((\Delta N^2)_0, (\Delta N^2)_1, \ldots, (\Delta N^2)_n)$, and $\mathbf{G}$ is a square matrix composed of the distances dy_{ij} and coefficient γ defined by (10.6).

Inverting $\mathbf{G}$, we can then determine the disturbance field knowing vertical displacements along a horizontal line:

$$\overrightarrow{\Delta N^2} = \mathbf{G}^{-1}\,\overrightarrow{\Delta z}. \tag{10.13}$$

If the image is placed well behind the tank, the components of $\mathbf{G}$ are somewhat more complicated because one must consider the angle at which light enters the tank from the image as well as the vertical displacement of light. The extra terms may be added to components of $\mathbf{G}$, akin to the inclusion of the second term in equation (10.10) for the spanwise-uniform problem [*Onu et al.*, 2003].

Note that computing $\Delta N^2(r)$ need only be done using image displacements rightward of the center of the disturbance. Independently, one can compute $\Delta N^2(r)$ using

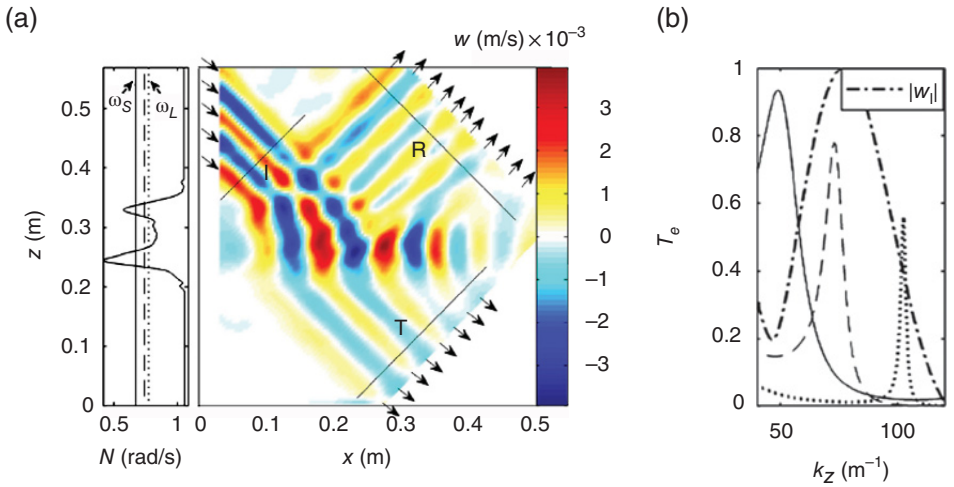

Figure 10.9. Schlieren image (color) showing the vertical velocity field associated with incident internal waves in nonuniformly stratified media partially transmitting (indicated by T) and reflecting (indicated by R) with partial trapping in a region of locally enhanced stratification for 0.27 m $\lesssim z \lesssim$ 0.33 m. The profile of the background stratification is shown on the left and transmission spectra are shown on the right for waves with frequencies indicated as the vertical lines through the buoyancy frequency profile shown (a). Adapted from Figure 3 of *Mathur and Peacock* [2010].

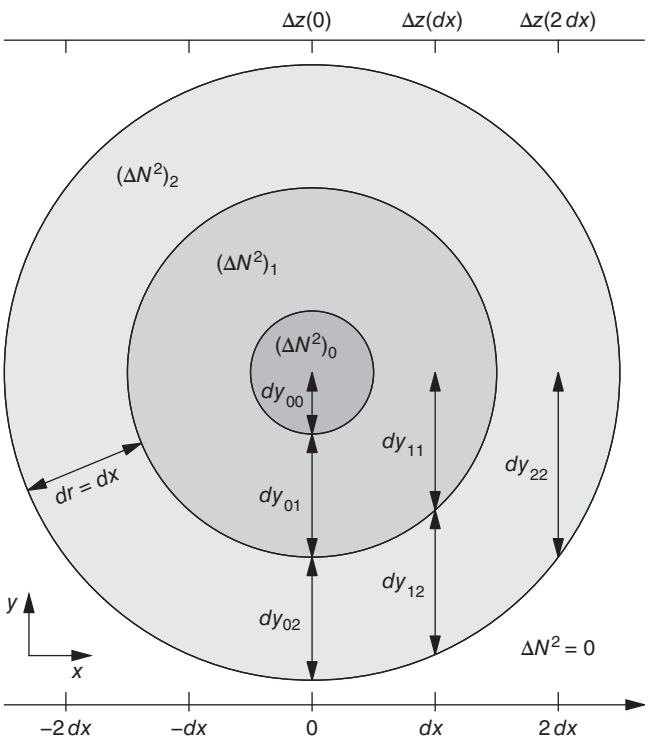

Figure 10.10. Discretization used to represent apparent displacements in an image behind a tank to axisymmetric disturbances within the tank. The disturbances are represented in terms of changes to the squared buoyancy frequency ΔN^2, which is assumed constant on annuli of width $dr = dx$, in which dx is the horizontal (e.g., pixel) resolution of the observed vertical displacements Δz of the object image.

image displacements leftward of center. Thus, comparing right and left gives a check on the accuracy of the assumption that the disturbance field was indeed axisymmetric.

Of course, the process of computing ΔN^2 at a particular height can be repeated at different heights so as to reconstruct a "snapshot" of $\Delta N^2(r, z)$. If the image is of dots instead of lines, one can compute horizontal as well as vertical components of the density gradient through this methodology.

An early application of axisymmetric schlieren examined the internal wave field surrounding a vertically oscillating sphere in uniformly stratified fluid [*Onu et al.*, 2003; *Flynn et al.*, 2003]. For example, Figure 10.11a shows the observed apparent vertical displacement of an image once the sphere had oscillated three times. No data were computed in the lower left-hand corner where the image was obscured by the sphere. The corresponding ΔN^2 field is shown in Figure 10.11b. As anticipated by theory, the along-beam amplitude decayed rapidly with distance from the center of the sphere as the conical wave beam expanded radially about the z axis. The theory predicted well the amplitude of the wave cones provided the sphere was sufficiently small (of radius 1.9 cm). But in experiments with a sphere of radius 3.2 cm, theory overpredicted the amplitude of the ΔN^2 field by as much as double, presumably because it neglected dynamics occurring within the viscous boundary layer surrounding the sphere [*Flynn et al.*, 2003].

This observation reveals a particularly useful aspect of the use of schlieren. Although the amplitude decays, the horizontal extent of the disturbance widens with distance from the origin. As a result, the vertical displacement

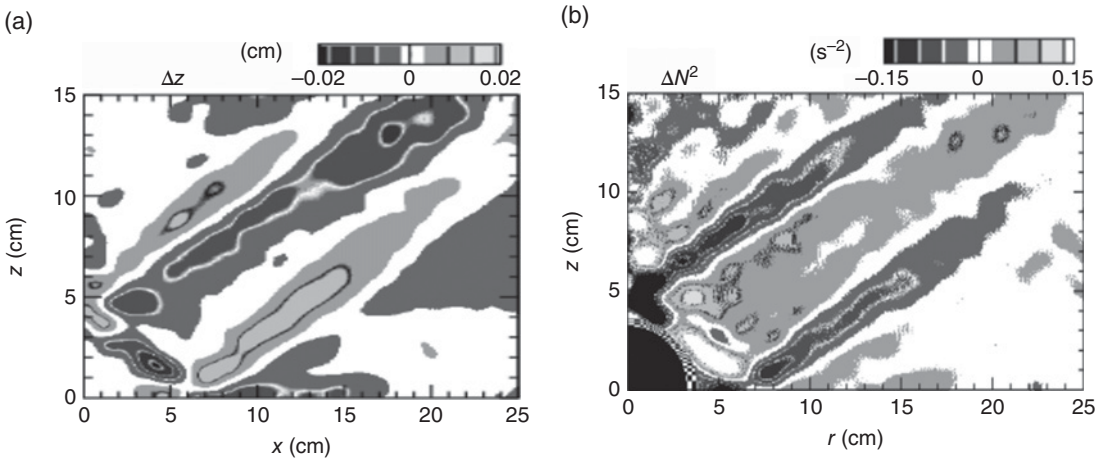

Figure 10.11. (a) Apparent vertical displacement $\Delta z(x, z)$ of horizontal lines in an image behind a tank in which a sphere (situated to the bottom left) oscillates in uniformly stratified fluid. (b) Corresponding change in squared buoyancy frequency $\Delta N^2(r, z)$ due to internal waves computed through axisymmetric synthetic schlieren. Adapted from Figures 2b and 4a of *Onu et al.* [2003].

signal does not weaken with distance away from the source. Indeed, the value of Δz in Figure 10.11a is largest near the top right-hand corner of the image. Hence, schlieren can extract signals over noise where in situ probe measurements or attempts to observe the motion of embedded particles might fail.

Since the development of the technique, it has been used to measure the laminar wake behind a falling sphere [*Yick et al.*, 2007] and internal waves above a plume in a stratified fluid [*Ansong and Sutherland*, 2010]. The latter case provided a model for internal wave generation by convective storms through the mechanical oscillator effect, in which the repeated rise and descent of cloud tops provide a forcing similar to that of an oscillating body.

10.4.2. Inverse Tomography

If the disturbance is fully three dimensional, then the problem of using synthetic schlieren to reconstruct the density gradient field from observed displacements of a single image is ill posed: Without invoking symmetry, it is impossible to reconstruct a three-dimensional object from its shadow. With multiple perspectives, however, it is possible to reconstruct and approximate the structure of the disturbance. In the medical use of magnetic resonance imaging (MRI), the method of tomographic reconstruction is well established. Making use of refractive index variations with air temperature, tomographic inversion has been used to measure the density of a supersonically expanding jet [*Faris and Byer*, 1988] and of two interacting jets [*Goldhahn and Seume*, 1988]. The latter was the first to employ the methodology of synthetic schlieren, recording the apparent displacement of an image of random dots, to determine the displacement of light rays.

Two approaches have since been taken to apply tomographic methods for the measurement of internal waves using synthetic schlieren. The Fourier-convolution approach of *Faris and Byer* [1988] and *Goldhahn and Seume* [1988] was used by *Hazewinkel et al.* [2011] in their study of internal wave attractors in a parabolic basin. The experiment itself was an extension of earlier studies into the formation of internal wave beams in spanwise-uniform, nonrectangular domains [*Maas et al.*, 1997; *Hazewinkel et al.*, 2008]. Because internal waves at a given frequency propagate at a fixed angle to the vertical, sloping sidewalls in the domain tend to focus the disturbances into a beam whose path effectively acts as an "attractor" for internal waves [*Maas and Lam*, 1995].

When a sphere was oscillated in stratified fluid within a paraboloidal basin, looking through the tank at different angles around the horizontal revealed attractor-like patterns in the observed displacement of images behind the tank. Four such images are shown in Figure 10.12. The information in these and several more images taken at different perspectives were combined through a convolution of their Fourier decompositions. The inverse transform of the result revealed the three-dimensional structure of the attractor, as shown in Figure 10.13.

A different approach follows that of the matrix inversion method used to measure axisymmetric disturbances [*Decamp et al.*, 2008]. At a fixed vertical level the observed image displacements could be represented by a vector with $2n$ entries, in which n is the number of pixels and the value is doubled to account for horizontal as well as vertical displacements. The perturbation density field (from which the density gradient is computed) could be discretized either in Cartesian or polar coordinates involving $N \equiv n_x \times n_y$ or $N \equiv n_r \times n_\theta$ points, respectively. For

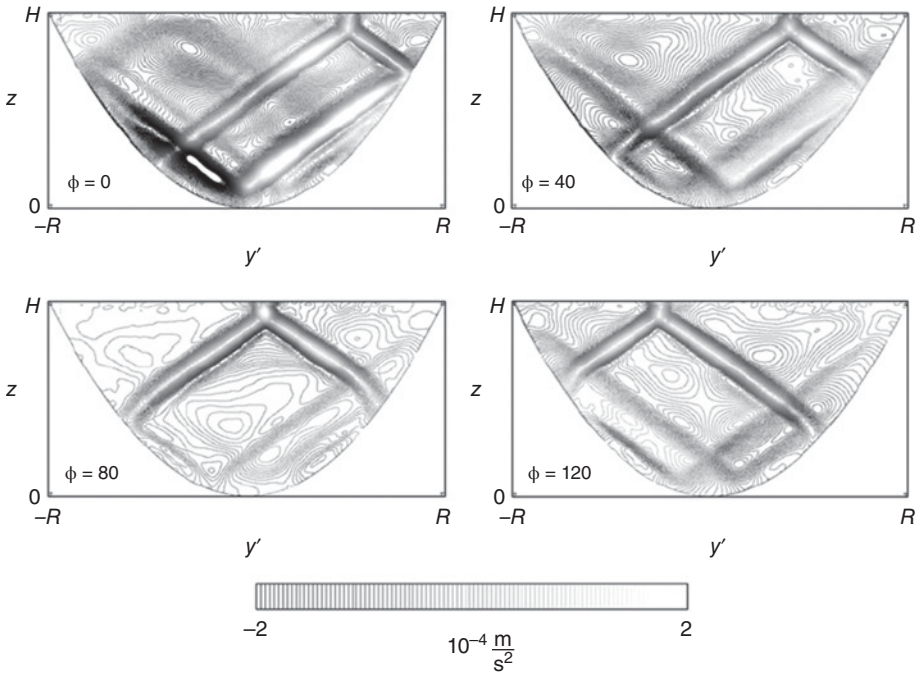

Figure 10.12. Image displacements recorded by different perspectives looking horizontally through a paraboloid filled with uniformly stratified fluid. The internal waves are generated by an oscillating sphere situated eccentrically near the surface. Reproduced from Figure 2 of *Hazewinkel et al.* [2011].

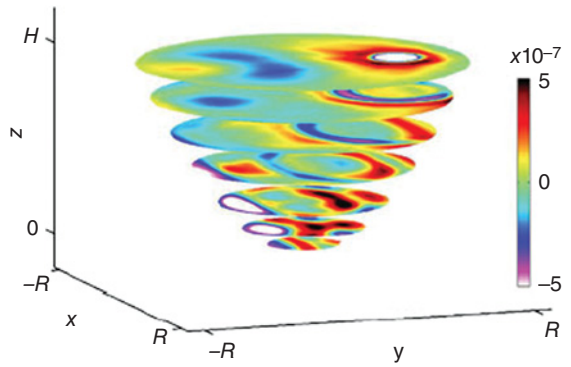

Figure 10.13. Tomographic reconstruction of internal wavefield inside a parabolic domain computed from many views of image displacements such as those in Figure 10.12. Reproduced from Figure 4a of *Hazewinkel et al.* [2011].

localized disturbances, the latter approach was found to be more effective.

The forward problem can thus be written as a coupled set of $2n$ equations in N unknowns. This is cast in matrix form analogous to equation (10.12):

$$\vec{\Delta} \equiv \left(\vec{\Delta x}^T, \vec{\Delta z}^T\right)^T = \mathbf{G}\,\vec{\rho}, \tag{10.14}$$

in which the differentiation operators acting on elements of ρ to give $\nabla\rho$ are buried inside the components of $\mathbf{G}$, which is a $2n$ — N rectangular matrix. The resolution of the disturbance is chosen so that there are more unknowns than equations. The typical method to solve this system of equations is to multiply through by the transpose, $\mathbf{G}^T$, thus recasting the problem as N equations in N unknowns. Because the N—N sparse matrix $\mathbf{G}^T\mathbf{G}$ is singular, it is typical to shift its eigenvalues by a so-called regularization parameter μ [*Zhdanov*, 2002]. Hence, the forward problem is written

$$\mathbf{G}^T\vec{\Delta} = \left(\mathbf{G}^T\mathbf{G} + \mu\mathbf{I}\right)\,\vec{\rho}, \tag{10.15}$$

in which $\mathbf{I}$ is the identity matrix.

Rather than compute the inverse of the matrix multiplying $\vec{\rho}$ on the right-hand side of (10.15), it is efficient to solve iteratively using the biconjugate gradient method [*Golub and van Loan*, 1996].

This approach was tested against idealized disturbances by *Decamp et al.* [2008], who showed that a polar grid is best used provided the number of sectors is not a multiple of the number of perspectives. Even with just six perspectives, a cosine-times-Gaussian disturbance was well reproduced on a polar grid with 33 sectors and 40 rings.

Applying this method to internal wave fields generated in the laboratory has proved challenging in part because of the requirement to have multiple perspectives. In the work of *Hazewinkel et al.* [2011], the tank had curved

sidewalls whose influence upon the path of light rays could be accounted for. In attempts to study non-axisymmetric waves generated (e.g., by a horizontally towed object) in a square tank, at most two perspectives at 90° might be recorded simultaneously, each with a camera on one side and the image on the other. To gain more perspectives, the experiment must be repeated but the generation mechanism reoriented within the tank to give the cameras a different perspective. This method requires perfect repeatability. Small changes can lead to large errors in the computation of $\nabla\rho$.

10.5. OTHER ADVANCES

Thus far we have focused upon the use of schlieren to examine internal waves in the laboratory. Here we mention other techniques used to generate and analyze internal waves.

10.5.1. Particle Image Velocimetry

Particle image velocimetry is now a well-established method used in the laboratory to measure flow fields nonintrusively. In this method, small particles are illuminated by a laser light sheet. Their displacements (or, more precisely, displacements of patches of particles in a window) are tracked between pulses of the laser. The technique has revolutionized laboratory experiments by providing a nonintrusive method that measures velocity at all points in the plane of the light sheet [*Fincham and Spedding*, 1997]. Using an oscillating mirror, one can also make multiple parallel light sheets that sequentially illuminate on a fast (typically microsecond) time scale [*Fincham*, 2006]. Thus the flow field can be reconstructed in three dimensions to within the resolution set by the separation between successive light sheets and the digital camera.

Using PIV in the study of internal waves poses additional challenges. Because light bends as it passes through stratified fluid, the position of particles in the flow can be misrepresented [*Dalziel et al.*, 2007]. One can try to eliminate particle distortions by adding another fluid to the ambient (e.g., alcohol) that cancels the refractive index change due to salinity, but this can also lead to problems with double diffusive behavior.

Without resorting to adding refractive index matching fluids, schlieren can be used to predict the distortion and so provide a correction to the digitized image of particles before they are processed to compute displacements.

For example, in the study of solitary waves by *Dalziel et al.* [2007], the direct application of PIV was hindered by distortions resulting from the sharp density gradient at the interface between the fresh and underlying salty water. Figure 10.14 shows the smearing and significant apparent particle displacement at a sharp density gradient. This is not due to the vertical motion of the wave. It results from photons between the laser light sheet and observer being deflected as they pass through the interface.

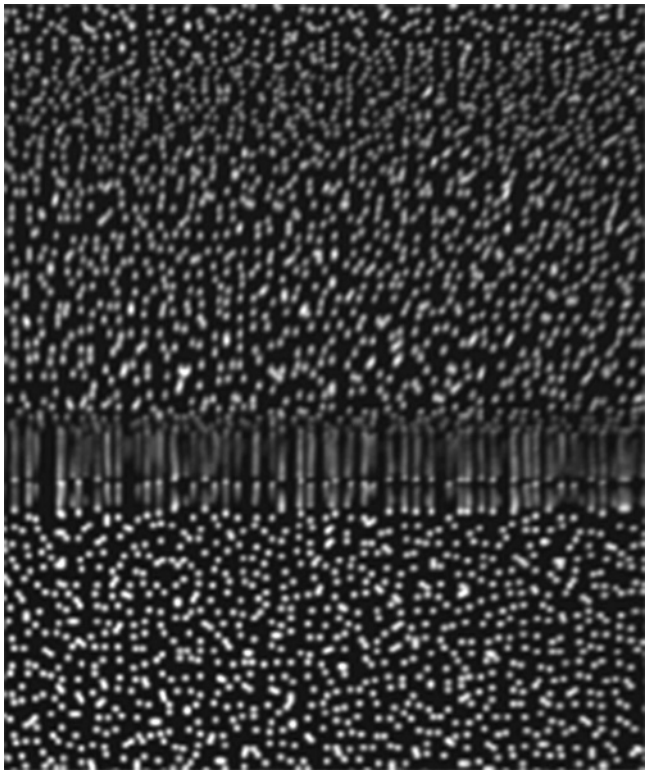

Figure 10.14. Image of random dots distorted by strong stratification at a density interface in an approximately two-layer fluid. Reproduced from Figure 6c of *Dalziel et al.* [2007].

Dalziel et al. [2007] addressed the issue by using schlieren to measure the density gradient and then using this information to correct for the apparent in situ particle displacement. The experimental configuration strobed between the camera recording the positions of particles in a laser light sheet in the fluid and it recording images of random dots on a screen behind the tank. This effectively rendered the schlieren and PIV measurements simultaneous. The result is shown in Figure 10.15. The corrected PIV image gives values of velocity and the schlieren measurements predicted the density. Importantly, the combined results measured the gradient Richardson number and so assessed the stability of internal solitary waves.

If the stratification is not too strong and disturbances in the fluid are not too large, then the distortion due to refractive index changes can be ignored and PIV can be applied directly. This method was used successfully in the measurement of internal waves generated by oscillatory flow over cylinders [*Zhang et al.*, 2007] spheres [*King et al.*, 2009] and a Gaussian-shaped hill [*Echeverri et al.*, 2009]. In these cases the distortions due to isopycnal

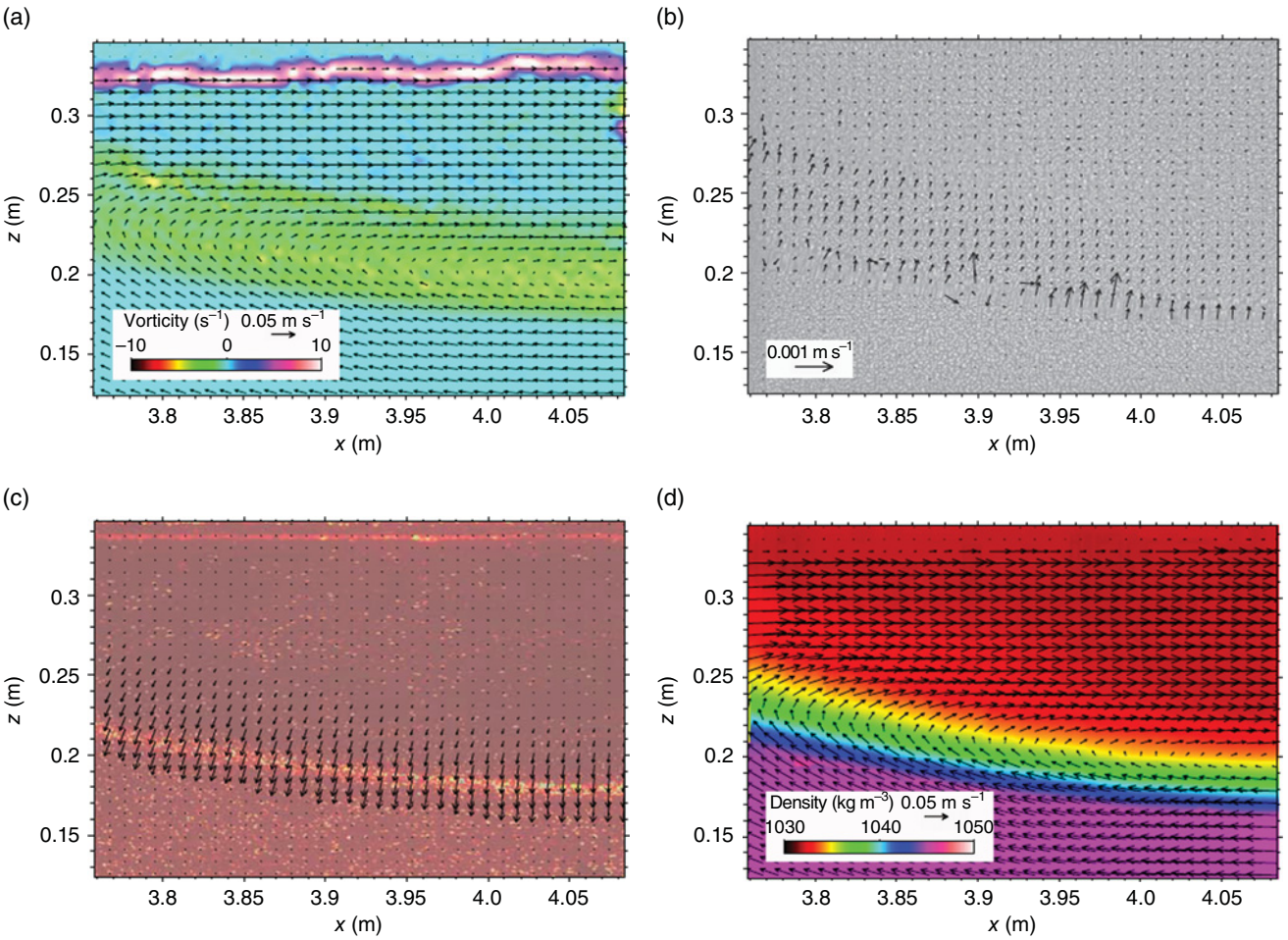

Figure 10.15. Combined PIV-schlieren examination of the passage of an internal solitary wave of depression in an approximately two-layer fluid. (a) Original velocity field computed using PIV superimposed on vorticity. (b) Apparent velocity resulting from distortions at density interface superimposed on background image of random dots. (c) Corrected displacements that account for strong density gradient at the interface superimposed on false color image of particles in the tank. (d) Corrected velocity field superimposed on contours of density. Reproduced from Figure 12 of *Dalziel et al.* [2007]. For color detail, please see color plate section.

displacements were not so large as to require corrections based upon schlieren.

An example of the use of PIV to measure internal wave amplitudes is shown in Figure 10.16. Here the color contours and arrows show the relative velocity field associated with internal waves generated when a Gaussian hill oscillated horizontally back and forth with maximum speed U. These are represented in a frame of reference moving with the hill, being equivalent to maximum flow rightward over the hill. In experiments (top images), the velocity could only be measured to the right of the hill. The structure of the beam is well reproduced by simulations (middle images) and theory, which predicts the far-field behavior (bottom images). This is true in subcritical cases (right), for which the slope of the wave beam is larger than the maximum slope of the hill, and in supercritical cases (left), for which the wave beam is tangent to the hill near its crest. The simulated amplitudes are smaller than what is observed, however. This can be attributed, in part, to the difficulty in capturing the viscous-dominated processes that occur in the generation region where the flow due to the waves moves along the hill slope. Coupling the nearly inviscid far-field dynamics with the viscous boundary layer dynamics remains an outstanding theoretical challenge.

10.5.2. "Fluo-Line" Technique

Laser-induced fluorescence is now frequently used in laboratory experiments to measure concentrations of fluorescent dye in the plane of a laser light sheet.

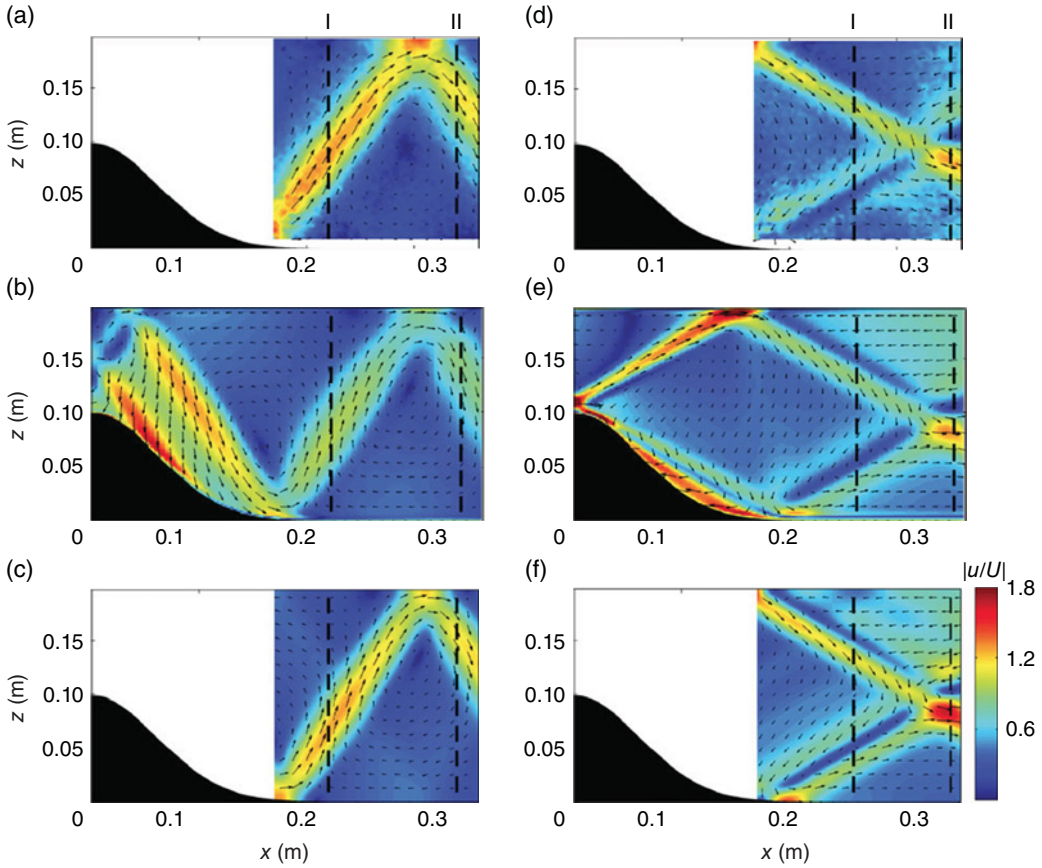

Figure 10.16. Experimental measurements (top), numerical results (middle), and theoretical predictions (bottom) of internal waves generated by oscillatory flow over a Gaussian hill in cases where the frequency of oscillation is subcritical (left) and supercritical (right). Reproduced from Figure 2 of *Echeverri et al.* [2009].

Consequently, this can be used to assess mixing and transport in fluids.

The technique has been used somewhat differently in the study of internal waves generated by a moving sphere in uniformly stratified fluid. Following the technique originally devised by of *Hopfinger et al.* [1991], *Voisin et al.* [2011] (see also *Ermanyuk et al.* [2011]) made thin, evenly spaced horizontal dye lines by soaking threads with fluorescein dye and slowly dragging them horizontally through a tank filled with uniformly stratified fluid. This created very thin markers of isopycnal surfaces that were clearly revealed as a sequence of lines in a vertical plane illuminated by a laser light sheet. The position of each line could be determined to subpixel accuracy by assuming a Gaussian vertical distribution of intensity.

An example of the displacement computed from successive dye lines in a plane passing through the center of a horizontally oscillating sphere is shown in Figure 10.17. Even where the displacement of lines is not obvious to the naked eye, they are clearly discerned by the digital analysis technique.

10.5.3. Novel Wave Generator

Typical methods for generating internal waves in the laboratory include oscillating a rigid body at constant frequency or towing a body horizontally at a constant speed. The former has the disadvantage that it creates four wave beams, as in Figure 10.2, or at least two if oscillated against a side boundary. Towed objects along a top or bottom boundary produce unidirectional waves, but towing piles up the stratified fluid ahead of the object forming what is called a "columnar mode." As a result, the endwall of the tank can influence the dynamics of flow over the obstacle [*Baines*, 1995].

A new mechanism for the generation of internal waves avoids these deficiencies [*Gostiaux et al.*, 2007; *Mercier et al.*, 2010]. In it vertically stacked flat plates periodically move back and forth providing forcing on the stratified fluid from the side. If the forcing is driven by a rotating spiral camshaft, as in Figure 10.18, the plates effectively move collectively as a vertically propagating wave whose vertical wavelength and amplitude are set by the

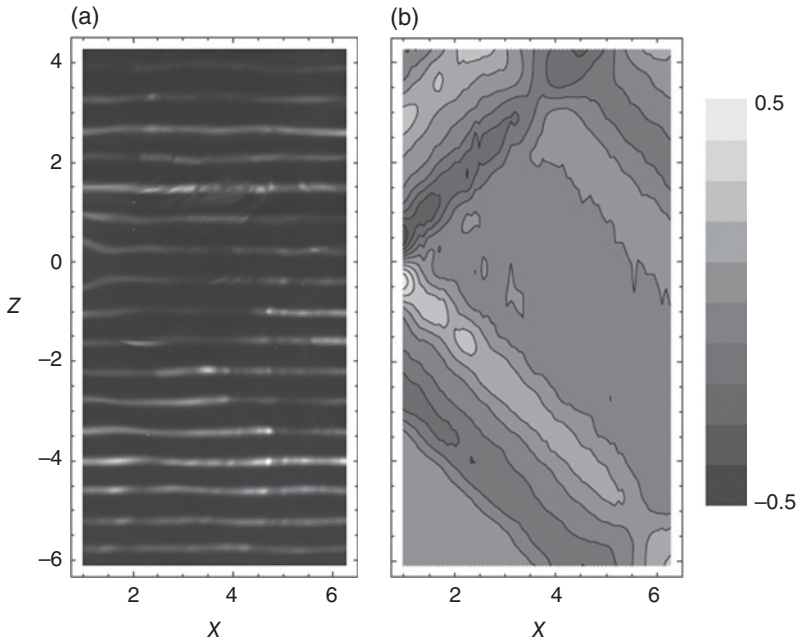

Figure 10.17. (a) Dye lines displaced to the right of a sphere oscillating horizontally about the origin in uniformly stratified fluid. (b) Computed displacement of the lines relative to the oscillating amplitude A. Reproduced from Figure 20 of *Voisin et al.* [2011].

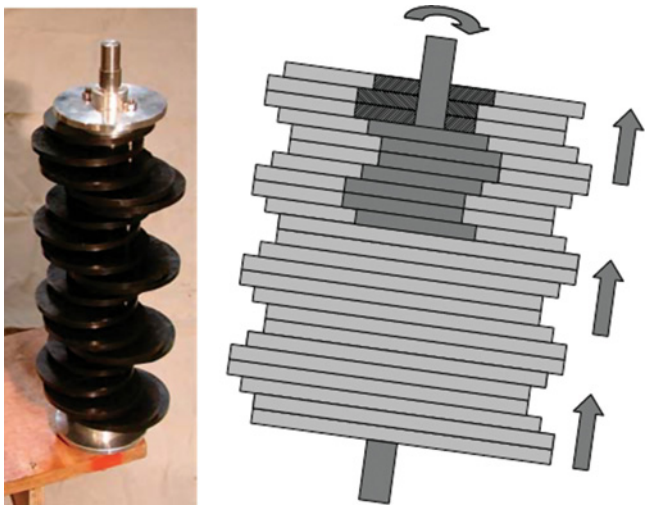

Figure 10.18. Camshaft and schematic cross section showing how the rotation of the shaft results in the back-and-forth oscillation of flat plates. Reproduced from Figure 2 of *Gostiaux et al.* [2007].

geometry of the camshaft and whose frequency is set by the rotation rate.

The mechanism thus acts like towed topography except that the translation of the periodic boundary is vertical. It does not generate columnar modes upstream. Nor is their boundary layer separation behind their crests. Because the boundary displacements are horizontal, large-amplitude forcing is less inclined to result in mixing of the stratified fluid.

This technique has been used in a variety of circumstances that have revealed important processes in the evolution of internal waves.

Satellite altimetry [*Egbert and Ray*, 2000] has recently been employed to observe the generation of oceanic internal waves by tidal flow over the continental margin and submarine sills. These have revealed the generation of low vertical-mode internal waves, associated with undulations of the thermocline. As well as theory and numerical simulations [*Balmforth et al.*, 2002; *Llewellyn-Smith and Young*, 2002; *Legg*, 2004], laboratory experiments have been performed to examine the generation of internal waves by Gaussian hill that oscillated horizontally back and forth with fixed frequency and amplitude [*Peacock et al.*, 2008; *Echeverri et al.*, 2009].

An outstanding question is how such low modes transfer their energy to smaller scales (high modes) so that they ultimately dissipate and mix the ocean.

The laboratory experiments by *Peacock et al.* [2009] examined one mechanism through which this may occur. When a low-mode internal wave is incident upon topography, the sloping sides of the hill refocus the energy into beams. This is shown in Figure 10.19.

The waves are created using the mechanism of oscillating stacked horizontal plates using the wave generator mechanism described above. Here, however, the rotating shaft is not spiral but is constructed with a vertically

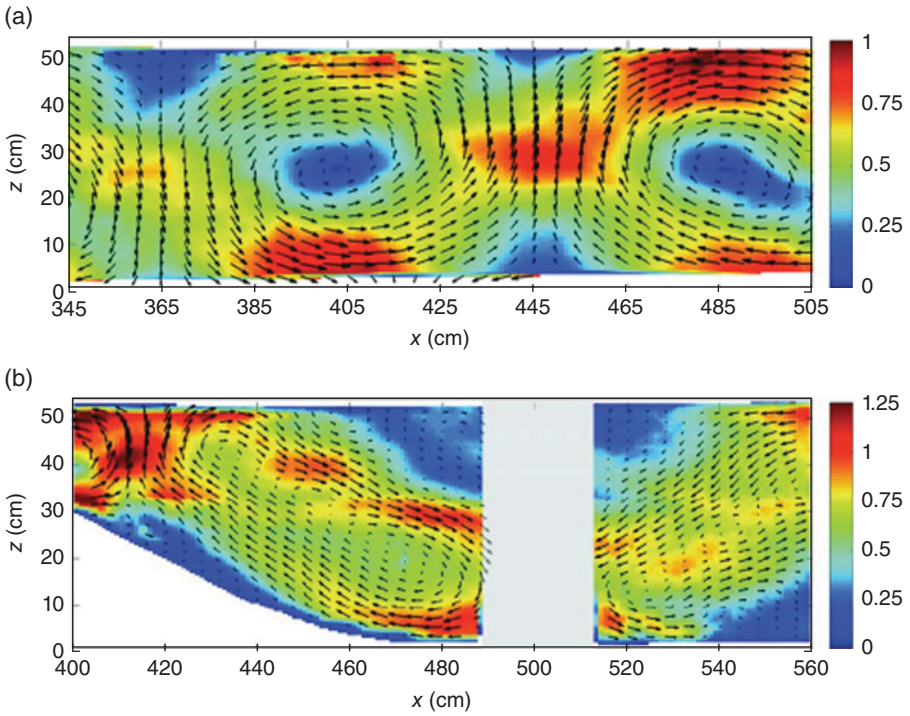

Figure 10.19. (a) Left-to-right propagating vertical mode 1 internal waves generated using horizontally oscillating flat plates, as in *Gostiaux et al.* [2007]. (b) Internal wave beam downstream of hill placed in front of the oncoming mode 1 waves. Adapted from Figures 2a and 3a of *Peacock et al.* [2009].

sinusoidal variation in a fixed plane so that rotating the shaft produces a mode 1 wave in a uniformly stratified medium [*Mercier et al.*, 2010]. In the absence of topography, PIV is used to reveal the mode 1 wave structure, which at one point in the phase exhibits forward motion at the surface and bottom and retrograde motion at mid depth. The flow directions reverse a half period later.

When this incident wavefield encounters a Gaussian hill, the structure of the wavefield changes significantly downstream. Just as an oscillating body creates internal wave beams in a stratified fluid, oscillations resulting from the incident low-mode internal waves create beamlike structures downstream. Thus energy from low modes is efficiently converted into higher modes. These ideas have recently been extended to the examination of internal waves incident upon the continental shelf [*Klymak et al.*, 2011].

10.6. DISCUSSION AND CONCLUSIONS

Several technological innovations have provided new tools for the study of internal waves in the laboratory. Here we have focused mostly upon the use of synthetic schlieren as a nonintrusive way to measure perturbation density gradients due to internal waves in continuously stratified media. When used to examine spanwise-uniform and axisymmetric disturbances, it has provided a useful check on the limitations of linear, inviscid theory, particularly with respect to the generation of internal waves from oscillating and steadily translating bodies.

Just as MRI revolutionized medicine, inverse tomography for schlieren has the potential to measure fully three-dimensional disturbances nonintrusively and continuously in time, provided the disturbances do not involve turbulent mixing and, hence, random scattering of light. However, several logistical obstacles remain to be overcome. In order to reconstruct relatively fine scale features, multiple perspectives from many angles must be recorded simultaneously or in rapid succession. But synthetic schlieren requires looking through a fluid at an object image on the opposite side. To have a large number of perspectives one must devise a method in which multiple cameras are not obstructed by multiple object images. Alternately, like MRI, one could construct a system in which the camera and object image rotate about a cylindrical tank on a fast time scale compared with that of internal waves. After image correction for the curvature of the tank there would remain the theoretical challenge to reconstruct the three-dimensional disturbance field from the images recorded continuously from changing perspectives.

PIV has provided another powerful tool for the nonintrusive examination of internal waves. It has the advantage of measuring in situ particle displacement, and hence velocities, in the plane of a laser light sheet. With multiple light sheets, the fully three-dimensional velocity field can be reconstructed within the spatial and temporal resolutions of the camera and laser.

Because light is significantly distorted where the refractive index changes due to rapid salinity changes, PIV is less effective at examining processes at density interfaces. However, synthetic schlieren and PIV can work in tandem, the former measuring density perturbations and using this information to predict how to correct the light distortion so that actual particle displacements can be measured more accurately through PIV.

To demonstrate the applications of schlieren and PIV, we have focused upon the phenomena of wave generation and propagation in nonuniform media. The dynamics of internal wave breaking with consequent mixing remains an outstanding challenge for experimentalists as well as theoretical and numerical modelers.

For example, in a process known as parametric subharmonic instability (PSI), internal waves resonantly transfer energy to subharmonic internal waves which may overturn and break or transfer energy to smaller-scale waves. PSI has been studied in laboratory experiments in which the displacement of horizontal dye lines were used to observe the evolution of resonantly excited mode 1 waves in a tank with square vertical cross section [*Benielli and Sommeria*, 1998]. The idealized numerical simulations of *MacKinnon and Winters* [2005] predicted that such resonance of internal tides might occur at 28.9°N latitude, which is the northern limit where subharmonic waves exist with frequencies lower than the inertial frequency f. Whether PSI actually occurs as catastrophically as they predicted in the ocean is presently under investigation. Laboratory experiments using the new technologies of schlieren and PIV may also provide new insights into the onset and energetics of PSI.

With increasing observations of internal solitary waves in the ocean, there is renewed interest in examining this phenomenon in the laboratory [*Grue et al.*, 2000; *Carr et al.*, 2008]. Although synthetic schlieren can work together with PIV to help correct apparent particle displacements within the flow [*Dalziel et al.*, 2007], it is not ideally suited to the study of interfacial waves. This is because the large curvature of the density field at the interface bends light to such a degree that an image behind the tank is distorted too much to compute apparent displacements.

Of course, one can track the motion of the interface by injecting dye there while the ambient is being established. The shadowgraph is also a useful tool. Other more innovative methods include the use of ultrasonic probes, which measure the interface displacement by recording the travel time of sound vertically through the ambient between a transmitter and receiver at a fixed depth straddling the interface [*Michallet and Barthélemy*, 1997, 1998].

Oceanographic observations continue to reveal the diversity and complexity of internal wave dynamics, sometimes inspiring and sometimes inspired by laboratory experiments. As digital cameras and image analyses continue to improve, the new techniques of schlieren and PIV are expected to continue stimulating new insights.

REFERENCES

Aguilar, D. A., and B. R. Sutherland (2006), Internal wave generation from rough topography, *Phys. Fluids*, *18*, Art. No. 066,603.

Alford, M. H., et al. (2011), Energy flux and dissipation in Luzon Strait: Two tales of two ridges, *J. Phys. Oceanogr.*, *41*, 2211–2222.

Ansong, J. K., and B. R. Sutherland (2010), Internal gravity waves generated by convective plumes, *J. Fluid Mech.*, *648*, 405–434.

Baines, P. G. (1974), The generation of internal tides over steep continental slopes, *Phil. Trans. R. Soc. Lond. A*, *277*, 27–58.

Baines, P. G. (1982), On internal tide generation models, *Deep-Sea Res.*, *29*, 307–338.

Baines, P. G. (1995), *Topographic Effects in Stratified Flows*, Cambridge Univ. Press, Cambridge, England.

Baines, P. G., and K. P. Hoinka (1985), Stratified flow over two-dimensional topography in fluid of infinite depth: A laboratory simulation, *J. Atmos. Sci.*, *42*, 1614–1630.

Balmforth, N. J., G. R. Ierley, and W. R. Young (2002), Tidal conversion by subcritical topography, *J. Phys. Oceanogr.*, *32*(10), 2900–2914.

Benielli, D., and J. Sommeria (1998), Excitation and breaking of internal gravity waves by parametric instability, *J. Fluid Mech.*, *374*, 117–144.

Bühler, O., and C. J. Muller (2007), Instability and focusing of internal tides in the deep ocean, *J. Fluid Mech.*, *588*, 1–28.

Carr, M., D. Fructus, J. Grue, A. Jensen, and P. A. Davies (2008), Convectively induced shear instability in large amplitude internal solitary waves, *Phys. Fluids*, *20*, 126,601, doi:10.1063/1.3030947.

Chashechkin, Y. D. (1999), Schlieren visualization of a stratified flow around a cylinder, *J. Vis.*, *1*, 345–354.

Dalziel, S. B., G. O. Hughes, and B. R. Sutherland (2000), Whole field density measurements, *Expt. Fluids*, *28*, 322–335.

Dalziel, S. B., M. Carr, J. K. Sveen, and P. A. Davies (2007), Simultaneous synthetic schlieren and PIV measurements for internal solitary waves, *Meas. Sci. Technol.*, *18*, 533–547.

Decamp, S., C. Kozack, and B. R. Sutherland (2008), Three-dimensional schlieren measurements using inverse tomography, *Expt. Fluids*, *20*, 747–758, doi:10.1007/s00348-007-0431-y.

Echeverri, P., M. R. Flynn, K. B. Winters, and T. Peacock (2009), Low-mode internal tide generation by topography: An experimental and numerical investigation, *J. Fluid Mech.*, *636*, 91–108.

Egbert, G. D., and R. D. Ray (2000), Significant dissipation of tidal energy in the deep ocean inferred from satellite altimeter data, *Nature*, *405*, 775–778.

Ermanyuk, E. V., J.-B. Flor, and B. Voisin (2011), Spatial structure of first and higher harmonic internal waves from a horizontally oscillating sphere, *J. Fluid Mech.*, *671*, 364–383.

Faris, G. W., and R. L. Byer (1988), Three-dimensional beam-deflection optical tomography of a supersonic jet, *Appl. Opt.*, *27*, 5202–5212.

Fincham, A., and G. Spedding (1997), Low cost, high resolution DPIV for measurement of turbulent fluid flow, *Expt. Fluids*, *23*, 449–462.

Fincham, A. M. (2006), Continuous scanning, laser imaging velocimetry, *J. Vis.*, *9*, 247–255.

Flynn, M. R., K. Onu, and B. R. Sutherland (2003), Internal wave generation by a vertically oscillating sphere, *J. Fluid Mech.*, *494*, 65–93.

Goldhahn, E., and J. Seume (1988), The background oriented schlieren technique: Sensitivity, accuracy, resolution and application to a three-dimensional density field, *Exp. Fluids*, *43*, 241–249.

Golub, G. H., and C. F. van Loan (1996), *Matrix computations*, 3rd ed., Johns Hopkins Univ. Press, London.

Görtler, H. (1943), Über eine schwingungserscheinung in flüssigkeiten mit stabiler dichteschichtung, *Z. Angew. Math. Mech.*, *23*, 65–71.

Gostiaux, L., H. Didelle, S. Mercier, and T. Dauxois (2007), A novel internal waves generator, *Exp. Fluids*, *42*, 123–130, doi:10.1007/s00348-006-0225-7.

Gregory, K., and B. R. Sutherland (2010), Transmission and reflection of internal wave beams, *Phys. Fluids*, *22*, Art. No. 106,601, doi:10.1063/1.3486613.

Grue, J., A. Jensen, P.-O. Rusas, and J. K. Sveen (2000), Breaking and broadening of internal solitary waves, *J. Fluid Mech.*, *413*, 181–217.

Hazewinkel, J., P. van Breevoort, S. B. Dalziel, and L. R. M. Maas (2008), Observations on the wavenumber spectrum and evolution of an internal wave attractor, *J. Fluid Mech.*, *598*, 373–382.

Hazewinkel, J., L. R. M. Maas, and S. B. Dalziel (2011), Tomographic reconstruction of internal wave patterns in a paraboloid, *Exp. Fluids*, *50*, 247–258.

Hopfinger, E. J., J.-B. Flor, J. M. Chomaz, and P. Bonneton (1991), Internal waves generated by a moving sphere and its wake in a stratified fluid, *Exp. Fluids*, *11*, 255–261.

Howes, W. L. (1984), Rainbow schlieren and its application, *Appl. Opt.*, *23*, 2449–2460.

Hurley, D. G. (1997), The generation of internal waves by vibrating elliptic cylinders. Part 1: Inviscid solution, *J. Fluid Mech.*, *351*, 105–118.

Hurley, D. G., and G. Keady (1997), The generation of internal waves by vibrating elliptic cylinders. Part 2: Approximate viscous solution, *J. Fluid Mech.*, *351*, 119–138.

King, B., H. P. Zhang, and H. L. Swinney (2009), Tidal flow over three-dimensional topography in a stratified fluid, *Phys. Fluids*, *21*, 116,601.

Klymak, J. M., and M. C. Gregg (2004), Tidally generated turbulence over the Knight Inlet sill, *J. Phys. Ocean.*, *34*(5), 1135–1151.

Klymak, J. M., R. Pinkel, C. T. Liu, A. K. Liu, and L. David (2006), Prototypical solitons in the South China Sea, *Geophys. Res. Lett.*, *33*(11), L11,607.

Klymak, J. M., M. H. Alford, R. Pinkel, R.-C. Lien, Y. J. Yang, and T.-Y. Tang (2011), The breaking and scattering of the internal tide on a continental slope, *J. Phys. Oceanogr.*, *41*, 926–945.

Koop, C. G., and B. McGee (1986), Measurements of internal gravity waves in a continuously stratified shear flow, *J. Fluid Mech.*, *172*, 453–480.

Larsen, L. H. (1969), Internal waves incident upon a knife edge barrier, *Deep Sea Res.*, *16*, 411–419.

Ledwell, J. R., E. Montgomery, K. Polzin, L. C. St. Laurent, R. Schmitt, and J. Toole (2000), Evidence for enhanced mixing over rough topography in the abyssal ocean, *Nature*, *403*, 179–182.

Legg, S. (2004), Internal tides generated on a corrugated slope. Part I: Cross-slope barotropic forcing, *J. Phys. Oceanogr.*, *34*, 156–173.

Li, Q., and D. M. Farmer (2011), The generation and evolution of nonlinear internal waves in the deep basin of the South China Sea, *J. Phys. Oceanogr.*, *41*, 1345–1363.

Lighthill, M. J. (1978), *Waves in Fluids*, Cambridge Univ. Press, Cambridge, England.

Llewellyn-Smith, S. G., and W. R. Young (2002), Conversion of the barotropic tide, *J. Phys. Oceanogr.*, *32*, 1554–1566.

Maas, L. R. M., and F.-P. A. Lam (1995), Geometric focusing of internal waves, *J. Fluid Mech.*, *300*, 1–41.

Maas, L. R. M., D. Benielli, J. Sommeria, and F.-P. A. Lam (1997), Observation of an internal wave attractor in a confined stably stratified fluid, *Nature*, *388*, 557–561.

MacKinnon, J. A., and K. B. Winters (2005), Subtropical catastrophe: Significant loss of low-mode tidal energy at 28.9°, *Geophys. Res. Lett.*, *32*, L15,605-1-5, doi:10.1029/2005GL023376.

Mathur, M., and T. Peacock (2009), Internal wave beam propagation in non-uniform stratifications, *J. Fluid Mech.*, *639*, 133–152.

Mathur, M., and T. Peacock (2010), Internal wave interferometry, *Phys. Rev. Lett.*, *104*, 118,501-1-4.

Meier, G. (2002), Computerized background oriented schlieren, *Exp. Fluids*, *33*, 181–187.

Mercier, M. J., N. B. Garnier, and T. Dauxois (2008), Reflection and diffraction of internal waves analyzed with the Hilbert transform, *Phy. Fluids*, *20*, Art. No. 086,601, doi:10.1063/1.2963136.

Mercier, M. J., D. Martinand, M. Mathur, L. Gostiaux, T. Peacock, and T. Dauxois (2010), New wave generation, *J. Fluid Mech.*, *657*, 308–334.

Michallet, H., and E. Barthélemy (1997), Ultrasonic probes and data processing to study interfacial solitary waves, *Exp. Fluids*, *22*, 380–386.

Michallet, H., and E. Barthélemy (1998), Experimental study of interfacial solitary waves, *J. Fluid Mech.*, *366*, 159–177.

Mowbray, D. E., and B. S. H. Rarity (1967), A theoretical and experimental investigation of the phase configuration of internal waves of small amplitude in a density stratified liquid, *J. Fluid Mech.*, *28*, 1–16.

Munk, W. H., and C. Wunsch (1998), Abyssal recipes II: Energetics of tidal and wind mixing, *Deep-Sea Res.*, *45*, 1977–2010.

Nault, J. T., and B. R. Sutherland (2007), Internal wave tunnelling across a mixed region, *Phys. Fluids*, *19*, 016,601-1-8, doi:10.1063/1.2424791.

Nault, J. T., and B. R. Sutherland (2008), Beyond ray tracing for internal waves. Part I: Small-amplitude anelastic waves, *Phys. Fluids*, *20*, 106,601-1-10, doi:10.1063/1.2993167.

Onu, K., M. R. Flynn, and B. R. Sutherland (2003), Schlieren measurement of axisymmetric internal wave amplitudes, *Expt. Fluids*, *35*, 24–31.

Peacock, T., P. Echeverri, and N. J. Balmforth (2008), An experimental investigation of internal tide generation by two-dimensional topography, *J. Phys. Oceanogr.*, *38*, 235–242.

Peacock, T., M. J. Mercier, H. Didelle, S. Viboud, and T. Dauxois (2009), A laboratory study of low-mode internal tide scattering by finite-amplitude topography, *Phys. Fluids*, *21*, Art. No. 121,702, doi:10.1063/1.3267096.

Pinkel, R. (2000), Internal solitary waves in the warm pool of the western equatorial Pacific, *J. Phys. Oceanogr.*, *30*, 2906–2926.

Polzin, K. L., J. M. Toole, J. R. Ledwell, and R. W. Schmitt (1997), Spatial variability of turbulent mixing in the Abyssal Ocean, *Science*, *276*, 93–96.

Robinson, R. M. (1969), The effects of a vertical barrier on internal waves, *Deep-Sea Res.*, *16*, 421–429.

Sandstrom, H. (1969), Effect of topography on propagation of waves in stratified fluids, *Deep Sea Res.*, *16*, 405–410.

Schardin, H. (1942), Die schlierenverfahren und ihre anwendungen, *Ergebnisse der Exakten Naturwissenschaften*, *20*, 303–439.

Settles, G. S. (2001), *Schlieren and Shadowgraph Techniques: Visualizing Phenomena in Transparent Media*, Springer Verlag, Berlin and New York.

Sutherland, B. R. (2002), Large-amplitude internal wave generation in the lee of step-shaped topography, *Geophys. Res. Lett.*, *29*(16), Art. No 1769.

Sutherland, B. R. (2010), *Internal Gravity Waves*, Cambridge Univ. Press, Cambridge.

Sutherland, B. R., and P. F. Linden (2002), Internal wave excitation by a vertically oscillating elliptical cylinder, *Phys. Fluids*, *14*, 721–731.

Sutherland, B. R., and K. Yewchuk (2004), Internal wave tunnelling, *J. Fluid Mech.*, *511*, 125–134.

Sutherland, B. R., S. B. Dalziel, G. O. Hughes, and P. F. Linden (1999), Visualisation and measurement of internal waves by "synthetic schlieren." Part 1: Vertically oscillating cylinder, *J. Fluid Mech.*, *390*, 93–126.

Teoh, S. G., G. N. Ivey, and J. Imberger (1997), Laboratory study of the interaction between two internal wave rays, *J. Fluid Mech.*, *336*, 91–122.

Thomas, N. H., and T. N. Stevenson (1972), A similarity solution for viscous internal waves, *J. Fluid Mech.*, *54*, 495–506.

Voisin, B. (1991), Internal wave generation in uniformly stratified fluids. Part 1. Green's function and point sources, *J. Fluid Mech.*, *231*, 439–480.

Voisin, B. (1994), Internal wave generation in uniformly stratified fluids. Part 2. Moving point sources, *J. Fluid Mech.*, *261*, 333–374.

Voisin, B., E. V. Ermanyuk, and J.-B. Flor (2011), Internal wave generation by oscillation of a sphere, with application to internal tides, *J. Fluid Mech.*, *666*, 308–357.

Weast, R. C. (1981), *Handbook of Chemistry and Physics*, 62nd ed., CRC. Press, Boca Raton, Fla.

Yick, K.-Y., R. Stoker, and T. Peacock (2007), Microscale synthetic schlieren, *Exp. Fluids*, *42*, 41–48.

Zeilon, N. (1912), On tidal boundary-waves and related hydrodynamical problems, *Handl. K. svenska Vetens. Akad.*, *47*, 1–46.

Zhang, H. P., B. King, and H. L. Swinney (2007), Experimental study of internal gravity waves generated by supercritical topography, *Phys. Fluids*, *19*, 096,602.

Zhdanov, M. (2002), *Geophysical Inverse Theory and Regularization Problems*, Elsevier, Amsterdam, New York, and Tokyo.